

# A blind deconvolution method for ground based telescopes and Fizeau interferometers

M. Prato<sup>a,\*</sup>, A. La Camera<sup>b</sup>, S. Bonettini<sup>c</sup>, S. Rebegoldi<sup>a</sup>, M. Bertero<sup>b</sup>, P. Boccacci<sup>b</sup>

<sup>a</sup>Dipartimento di Scienze Fisiche, Informatiche e Matematiche, Università di Modena e Reggio Emilia, Via Campi 213/b, 41125 Modena, Italy

<sup>b</sup>Dipartimento di Informatica, Bioingegneria, Robotica e Ingegneria dei Sistemi, Università di Genova, Via Dodecaneso 35, 16145 Genova, Italy

<sup>c</sup>Dipartimento di Matematica e Informatica, Università di Ferrara, Via Saragat 1, 44122 Ferrara, Italy

---

## Abstract

In the case of ground-based telescopes equipped with adaptive optics systems, the point spread function (PSF) is only poorly known or completely unknown. Moreover, an accurate modeling of the PSF is in general not available. Therefore in several imaging situations the so-called blind deconvolution methods, aiming at estimating both the scientific target and the PSF from the detected image, can be useful. A blind deconvolution problem is severely ill-posed and, in order to reduce the extremely large number of possible solutions, it is necessary to introduce sensible constraints on both the scientific target and the PSF.

In a previous paper we proposed a sound mathematical approach based on a suitable inexact alternating minimization strategy for minimizing the generalized Kullback-Leibler divergence, assuring global convergence. In the framework of this method we showed that an important constraint on the PSF is the upper bound which can be derived from the knowledge of its Strehl ratio. The efficacy of the approach was demonstrated by means of numerical simulations.

In this paper, besides improving the previous approach by the use of a further constraint on the unknown scientific target, we extend it to the case of multiple images of the same target obtained with different PSFs. The main application we have in mind is to Fizeau interferometry. As it is known this is a special feature of the Large Binocular Telescope (LBT). Of the two expected interferometers for LBT, one, LINC-NIRVANA, is forthcoming while the other, LBTI, is already operating and has provided the first Fizeau images, demonstrating the possibility of reaching the resolution of a 22.8 m telescope. Therefore the extension of our blind method to this imaging modality seems to be timely.

The method is applied to realistic simulations of imaging both by single mirrors and Fizeau interferometers. Successes and failures of the method in the imaging of stellar fields are demonstrated in simple cases. These preliminary results look promising at least in specific situations. The IDL code of the proposed method is available on request and will be included in the forthcoming version of the Software Package AIRY (v.6.1).

**Keywords:** blind deconvolution, numerical optimization, image reconstruction, Fizeau interferometers

---

## 1. Introduction

In a previous paper (Prato et al., 2013) we proposed a blind deconvolution method for ground-based telescopes equipped with an adaptive optics (AO) system. Assuming that the image and the corresponding background are known, then the features of the method are the following:

- formulation of the problem as a constrained minimization of the data fidelity function in the case of Poisson noise (photon counting), namely a generalized Kullback-Leibler divergence depending on the unknown astronomical target (in the following called the *object*) and on the unknown point spread function (PSF);
- non-negativity of the object;

- non-negativity of the PSF and normalization to unit volume;
- upper bound on the PSF values derived from the knowledge of the Strehl ratio (SR), as suggested by Desiderà and Carillet (2009);
- use of the inexact alternating minimization method proposed by Bonettini (2011) and based on the *scaled gradient projection* (SGP) method (Bonettini et al., 2009; Prato et al., 2012).

The method is iterative and at each outer iteration the object and the PSF are updated by means of given (but arbitrary) numbers of inner iterations of SGP. We remark that when SGP is applied to the object only projection on the non-negative orthant is required while, in the case of the PSF, the projection is performed on the convex and closed set defined by the box and equality constraints.

Our proposed method is similar to blind methods based on the Richardson-Lucy (RL) algorithm (Richardson, 1972; Lucy, 1974) or its accelerated versions, such as those proposed in Holmes (1992); Tsumuraya et al. (1994); Fish et al. (1995);

---

\*Corresponding author. Tel.: +39 059 2055590; fax: +39 059 370513.

Email addresses: marco.prato@unimore.it (M. Prato), andrea.lacamera@unige.it (A. La Camera), silvia.bonettini@unife.it (S. Bonettini), simone.rebegoldi@unimore.it (S. Rebegoldi), bertero@unige.it (M. Bertero), patrizia.boccacci@unige.it (P. Boccacci)

Biggs and Andrews (1998) for the case of single image and in Desiderà et al. (2006) for the case of multiple images, applicable to Fizeau interferometry. But the advantage of using SGP in place of RL is double: first, as proved in Bonettini (2011), global convergence of the iteration holds true, i.e. any limit point of the sequence is a stationary point of the constrained KL divergence; secondly it is possible to introduce box and equality constraints on the different blocks of variables (object and PSF).

Therefore the novelty of the method is that it is based on a sound mathematical approach and allows, in an easy way, the introduction of important constraints on the PSF such as the Strehl constraint, preventing the appearance of trivial solutions such as a delta function.

The method, in its present form, does not consider the use of regularization for the object or the PSF, in addition to that provided by the constraints mentioned above. We remark that it is quite easy to introduce as an additional constraint on the object the value of its flux (namely, its  $\ell_1$  norm), as derived from the detected images and the knowledge of the background. This constraint, enforcing the sparsity of the object, is considered in this paper. If we select a large number of inner iterations on the object variables, the method is suitable for the reconstruction of star systems, as already remarked in Prato et al. (2013); this result is confirmed in this paper by means of simulations more realistic than those used in that paper.

However the main contribution of this paper is the extension of the method to the case of Fizeau interferometry. As it is known this is a specific feature of the Large Binocular Telescope which consists of two 8.4 m mirrors situated on a common mount with a center to center distance of 14.4 m. Indeed, this structure is suitable for Fizeau interferometry which should provide images with the resolution of a 22.8 m telescope in the direction of the baseline joining the center of the two mirrors and that of a 8.4 m telescope in the orthogonal direction. Different images of the same target corresponding to different orientations of the baseline can be combined by suitable deconvolution methods to provide a unique reconstructed image with the highest resolution in all directions (Bertero et al., 2011).

Two interferometers are planned for LBT: the forthcoming LINC-NIRVANA (Herbst et al., 2003), in advanced realization stage by a German-Italian consortium led by MPIA, Heidelberg, and the NASA funded LBTI (Wilson et al., 2008; Bailey et al., 2014) already operating on Mount Graham. Indeed, images of the Jupiter moon Io were obtained with LBTI/LMIRcam during UT 2013 December 24, showing that the resolution of a 22.8 m is reachable (Leisenring et al., 2014) and thus proving that LBT is the first in a class of extremely large telescopes (ELT).

All the methods developed for Fizeau interferometry are also applicable to other situations where multiple images of the same target, corresponding to different PSFs, are available such as the co-adding problem in Astronomy (Lucy and Hook, 1992) or the multiple image method used in STED microscopy for improving the signal-to-noise ratio (Castello et al., 2014).

For this reason we present in Sect. 2 our blind method without a specific reference to Fizeau interferometry but just as a

method for multiple image deconvolution in the case of Poisson noise, including, as it is obvious, the case of a single image as a particular case. In the same section we discuss the intrinsic limitations of our constrained blind deconvolution, a discussion which is possible in our sound mathematical framework.

In the simulations intended to validate the method we focus on LBT which is equipped with a very innovative AO system, the so-called First Light AO (FLAO) system (Esposito et al., 2010), providing SR values up to 0.9 in K-band. Therefore for single image simulations we use models of the PSF of such a system. On the other hand, for multiple image deconvolution we consider images generated by means of PSFs computed for the interferometer LINC-NIRVANA (LN) in K band. Since the camera of LINC-NIRVANA has a pixel size of  $\sim 5$  mas while the LMIRcam of LBTI has a pixel size of 10.7 mas, the shape of the PSFs of LN in K band ( $2.2\mu\text{m}$ ) is similar to the shape of the PSFs of LBTI in M band ( $4.8\mu\text{m}$ ). Obviously the properties of the images may be very different. Details on image modeling and simulation are given in Sect. 3.

Finally in Sect. 4 we discuss our numerical results in the case of binary systems and “open cluster” models. Conclusions are sketched in Sect. 5.

## 2. Method

We assume that  $p$  different images of the scientific object, with  $p$  different PSFs are available. The case of a single aperture telescope obviously corresponds to  $p = 1$  if only one image has been acquired; if different observations have been performed at different times, hence with PSFs corresponding to different AO corrections, then the approach can be used for the co-adding of these images.

Let  $\mathbf{f}$  be the unknown astronomical object and let  $\mathbf{K}_j$  be the unknown PSFs (each one normalized to unit volume) corresponding to the detected images  $\mathbf{g}_j$  for  $j = 1, \dots, p$  (we assume for simplicity a space-invariant model), then we define as  $A_j \mathbf{f} = \mathbf{K}_j * \mathbf{f}$  the corresponding imaging matrices. Moreover we denote as  $\mathbf{b}_j$  the expected value of the background emission in image  $\mathbf{g}_j$  and we assume that it is known, so that the expected value of  $\mathbf{g}_j$  is given by  $A_j \mathbf{f} + \mathbf{b}_j$ .

Since it is quite natural to assume that the  $p$  images are statistically independent, the likelihood of the problem is the product of the likelihoods of the different images. We assume that they are perturbed by Poisson noise. Then, by taking the negative logarithm of the likelihood we obtain the following data-fidelity function which is the sum of  $p$  Kullback-Leibler (KL) generalized divergences, also known as Csiszár I-divergences (Csiszár, 1991), one for each image, i.e.

$$J_0(\mathbf{f}, \mathbf{K}_1, \dots, \mathbf{K}_p; \mathbf{g}, \mathbf{b}) = \sum_{j=1}^p \sum_{\mathbf{m} \in S} \left\{ \mathbf{g}_j(\mathbf{m}) \ln \frac{\mathbf{g}_j(\mathbf{m})}{(A_j \mathbf{f})(\mathbf{m}) + \mathbf{b}_j(\mathbf{m})} + (A_j \mathbf{f})(\mathbf{m}) + \mathbf{b}_j(\mathbf{m}) - \mathbf{g}_j(\mathbf{m}) \right\}, \quad (1)$$

where  $S$  is the set of the values of the multi-index  $\mathbf{m}$  characterizing the pixels of the image array, and  $(\mathbf{g}, \mathbf{b}) = \{(\mathbf{g}_j, \mathbf{b}_j)\}_{j=1}^p$ .

The problem of image deconvolution (without regularization) consists in the minimization of this function with respect to  $\mathbf{f}$  for given PSFs, images and backgrounds. The minimization can be obtained by means of RL in the single image case, by means of OS-EM method (Hudson and Larkin, 1994; Bertero and Boccacci, 2000) in the multiple image case, or by means of SGP method (Bonettini et al., 2009; Prato et al., 2012) in both cases. As shown in Prato et al. (2012) SGP is more efficient than OS-EM if the number  $p$  of images is not too large.

### 2.1. Blind deconvolution: problem formulation

If images and backgrounds are given, the ML approach to blind deconvolution can be formulated as the minimization of the function in Eq. (1) with respect to  $p + 1$  blocks of unknown variables, namely the object  $\mathbf{f}$  and the  $p$  PSFs  $\mathbf{K}_j$ ,  $j = 1, \dots, p$ . As it is known, this function is convex with respect to each block of variables for fixed values of the others, but is not convex with respect to the full set of variables (Prato et al., 2013). Therefore blind deconvolution is a difficult problem of nonconvex optimization. Moreover, this problem is highly ill-posed and allows uninteresting solutions. For instance, a global minimum can be achieved by choosing  $\mathbf{f} = \mathbf{g} - \mathbf{b}$  and  $\mathbf{K}_j = \delta$ ,  $j = 1, \dots, p$ , where  $\delta$  is the Dirac delta array. This trivial minimizer can be avoided by the introduction of suitable regularization terms and constraints.

Since we mainly consider the case of stellar fields or, in other words, of sparse objects, by taking into account the sparsity property of the minimizers of the KL divergence in the case of image deconvolution (Bertero et al., 2009), we do not introduce an object-dependent regularization term in the objective function. However, besides non-negativity of the object we also introduce a constraint on its flux; more precisely we require that the object flux coincides with the average flux of the  $p$  detected images (after background subtraction), which is given by

$$c = \frac{1}{p} \sum_{j=1}^p \sum_{\mathbf{m} \in S} \{g_j(\mathbf{m}) - b_j(\mathbf{m})\} . \quad (2)$$

We remark that this constraint is further enforcing sparsity; in the case of deconvolution and zero value of the backgrounds, it is automatically satisfied by the minimizers of the KL divergence.

As concerns the PSFs, as shown in Desiderà and Carbillat (2009) and Prato et al. (2013), an important constraint is the upper bound derived from the knowledge of the SR characterizing the AO correction of the atmospheric blur during the observation. Moreover, non-negativity and normalization provide additional constraints. In conclusion, the nonconvex optimization problem we are considering can be formulated as follows

$$\begin{aligned} \min \quad & J_0(\mathbf{f}, \mathbf{K}_1, \dots, \mathbf{K}_p; \mathbf{g}, \mathbf{b}) \\ \text{s.t.} \quad & \mathbf{f} \geq 0, \quad \sum_{\mathbf{n} \in S} \mathbf{f}(\mathbf{n}) = c; \\ & 0 \leq \mathbf{K}_j \leq s_j, \quad \sum_{\mathbf{n} \in S} \mathbf{K}_j(\mathbf{n}) = 1; \quad j = 1, \dots, p, \end{aligned} \quad (3)$$

where  $s_j$  is the upper bound on the PSF  $\mathbf{K}_j$  derived from the knowledge of the SR characterizing the acquisition of  $\mathbf{g}_j$ . In conclusion the data of the problem are  $(\mathbf{g}, \mathbf{b})$  and  $s = \{s_j\}_{j=1}^p$ .

Another important constraint can be provided by the requirement of band-limiting of the PSFs, which is used for instance in Desiderà et al. (2006). Indeed the band of the PSF, i.e the set in Fourier space where the Fourier transform of the PSF is not zero, is known and consists, in general, of a disc in the case of a single aperture telescope and a union of three discs in the case of a Fizeau interferometer with LBT, the central one being the band of the mirrors of LBT and the side-ones the replicas due to interferometry (see, for instance, Bertero et al., 2011). This constraint on the Fourier transform of the PSF, together with normalization and upper and lower bounds, defines a convex set. Unfortunately, since we use projection methods, the projection of an array on this set is not easily computable, even if methods for computing the projection on the intersection of convex sets are available. The difficulty is that these methods are not efficient and therefore can lead to an excessive computational cost since the projection should be computed several times in the used iterative methods. However, from the numerical experiments described in Prato et al. (2013) we deduce that a suitable initialization of our algorithm, based on a PSF satisfying the band constraint, may lead to a set of reconstructed PSFs whose bands are very close to the desired ones.

### 2.2. Blind deconvolution: alternating minimization

Although the previous formulation of blind deconvolution requires the minimization of a nonconvex objective function, the constraints have a nice separable structure, since they involve separately the blocks of variables, defining a feasible convex set for each of them. In addition, the function is convex with respect to the different blocks of variables. In these settings, the solution of problem (3) can be sought by means of an *alternating minimization* (AM) strategy.

The basic idea of AM is the cyclic minimization for the constrained problem with respect to one block of variables, updating its value for the next minimization step. This kind of approach is known in the literature also as *nonlinear Gauss-Seidel* or *block coordinate descent* method and its theoretical properties have been deeply studied in the last decades (Bertsekas, 1999; Grippo and Sciandrone, 1999, 2000; Luo and Tseng, 1992).

In our case, each iteration of the AM method consists in solving the following  $p + 1$  constrained minimization problems of convex functions

$$\begin{aligned} \mathbf{f}^{(k+1)} &= \arg \min_{\mathbf{f} \in \Omega} J_0(\mathbf{f}, \mathbf{K}_1^{(k)}, \dots, \mathbf{K}_p^{(k)}; \mathbf{g}, \mathbf{b}) \\ \mathbf{K}_1^{(k+1)} &= \arg \min_{\mathbf{K} \in \Omega_1} J_0(\mathbf{f}^{(k+1)}, \mathbf{K}, \dots, \mathbf{K}_p^{(k)}; \mathbf{g}, \mathbf{b}) \\ &\vdots \\ \mathbf{K}_p^{(k+1)} &= \arg \min_{\mathbf{K} \in \Omega_p} J_0(\mathbf{f}^{(k+1)}, \mathbf{K}_1^{(k+1)}, \dots, \mathbf{K}; \mathbf{g}, \mathbf{b}), \end{aligned} \quad (4)$$

where  $k$  is an index running on the AM iterations,  $\Omega$  is the set of the constraints on the object  $\mathbf{f}$  and  $\Omega_j$  is the set of the constraints on the PSF  $\mathbf{K}_j$ . The limit points of the sequence generated by this iteration scheme are also stationary points for the

constrained problem if each partial problem is the minimization of a strictly convex function (Bertsekas, 1999). This condition is not only sufficient but also necessary when more than two blocks of variables are involved. Indeed, Powell (1973) showed a counterexample where the strict convexity is not satisfied, three blocks of variables are involved and the AM method fails to locate stationary points.

Even when the hypothesis of strict convexity on each block of variables holds true, the convergence of the AM scheme can be proved only if each partial minimization problem is solved *exactly*, which is often impractical or too costly (in general iterative methods are used). Quite surprisingly the convergence result is obtained without the assumption of strict convexity if SGP is used for solving inexactly the partial minimization problems. This important result is proved in Bonettini (2011) and is basic for the proposed approach to blind deconvolution.

In conclusion, at each line of Eq. (4) the minimization is replaced by a given number of SGP iterations. These will be called *inner* iterations while the iterations of the AM scheme will be called *outer* iterations. Therefore the sequence generated by the method depends both on the initialization of the first outer iteration (in the subsequent outer iterations the inner iterations are initialized with the results derived from the previous one) and on the given numbers of inner iterations for each block of variables. In the present application it seems quite natural to choose the same number of inner iterations for all the PSF's blocks.

### 2.3. SGP algorithm

Since it is basic for the solution of the partial minimization problems it may be useful to briefly recall the main points of the SGP algorithm (Bonettini et al., 2009) even if its application to astronomical imaging has already been described elsewhere (Prato et al., 2012; Bonettini and Prato, 2010, 2014). To this purpose we remark that each minimization problem in the iterative scheme of Eq. (4) has the following structure

$$\min_{\mathbf{h} \in \Omega} J_0(\mathbf{h}) , \quad (5)$$

where, for simplicity, we omitted the dependence on the other variables and  $\Omega$  is the closed and convex set defined by the constraints. The main difference with respect to Prato et al. (2012) is that  $\Omega$  is a subset of the non-negative orthant defined by a suitable equality constraint. Therefore the projection on this set is more complex than that on the non-negative orthant.

The main step of SGP is the computation of the  $k$ -th feasible descent direction (where  $k$  is an index running on the inner iterations of a given AM iteration)

$$\mathbf{d}^{(k)} = P_{\Omega, D_k^{-1}}(\mathbf{h}^{(k)} - \alpha_k D_k \nabla J_0(\mathbf{h}^{(k)})) - \mathbf{h}^{(k)}$$

by performing the following steps:

- a) The direction provided by the negative gradient  $-\nabla J_0(\mathbf{h}^{(k)})$  is modified by a diagonal scaling matrix  $D_k$  with positive entries, which in all the subproblems of one AM iterations is given by

$$D_k = \text{diag}(\min(L_2, \max(L_1, \mathbf{h}^{(k)})) , \quad (6)$$

$(L_1, L_2)$  being given constants estimated from the extreme values of the image.

- b) A point on the scaled gradient direction is selected by choosing a multiplicative factor  $\alpha_k$  by means of an alternation of the generalized Barzilai-Borwein (BB) rules (Barzilai and Borwein, 1988; Bonettini et al., 2009)

$$\alpha_k^{(BB1)} = \frac{(\mathbf{s}^{(k-1)})^T D_k^{-1} D_k^{-1} \mathbf{s}^{(k-1)}}{(\mathbf{s}^{(k-1)})^T D_k^{-1} \mathbf{z}^{(k-1)}} , \quad (7)$$

$$\alpha_k^{(BB2)} = \frac{(\mathbf{s}^{(k-1)})^T D_k \mathbf{z}^{(k-1)}}{(\mathbf{z}^{(k-1)})^T D_k D_k \mathbf{z}^{(k-1)}} ,$$

where  $\mathbf{s}^{(k-1)} = \mathbf{h}^{(k)} - \mathbf{h}^{(k-1)}$  and  $\mathbf{z}^{(k-1)} = \nabla J_0(\mathbf{h}^{(k)}) - \nabla J_0(\mathbf{h}^{(k-1)})$ , and a suitable introduction of upper and lower bounds.

- c) The resulting point is brought back in the feasible set  $\Omega$  by means of the projection  $P_{\Omega, D_k^{-1}}$  associated to the norm induced by  $D_k^{-1}$ , i.e.

$$P_{\Omega, D_k^{-1}}(\mathbf{h}) = \arg \min_{\mathbf{y} \in \Omega} (\mathbf{h} - \mathbf{y})^T D_k^{-1} (\mathbf{h} - \mathbf{y}). \quad (8)$$

Since the feasible sets of both the object and the PSFs involve a given number of inequalities plus an equality constraint, in all cases we used a secant-based routine developed by Dai and Fletcher (2006), which is able to compute the projection with a computational cost growing linearly in time with respect to the image size (see also Prato et al., 2013).

### 2.4. Discussion

In the previous approach, the blind deconvolution problem is formulated as the constrained minimization of a nonconvex function which depends on an extremely large number of variables, about  $10^6$  in the numerical experiments described in this paper. Since the constraints used in our approach imply that the sequences of objects and PSFs generated by the inexact AM method are bounded, it follows that these sequences have limit points. We can add that, even if it is difficult to provide a theoretical evidence of the existence of a unique limit point, in all our numerical experiments the sequences produced by the inexact AM method have a convergent behaviour. However, according to the general convergence result proved in Bonettini (2011), we can only state that the limit points are *stationary points* of the function, hence not necessarily minimizers.

As far as we know, there is no practical way for establishing if these points are minimizers or not. In fact, it should be necessary to manage the Hessian of the function in these points but this is an absolutely intractable matrix even if one can write it explicitly (Prato et al., 2013). Since one can use different initializations of the iterative procedure and different numbers of inner iterations and these different choices can produce different results, in a practical application we do not see an approach better than that of doing different attempts and look for that providing the most sensible solution.

An additional difficulty is that it may happen, as we show by some numerical simulations, that a sensible solution corresponds to a value of the objective function which is greater than the value of the same function corresponding to a solution which is clearly unphysical. It is obvious that these situations should not be surprising because the problem of blind deconvolution is nonconvex and therefore the objective function can have several local minimizers as well as stationary points. Since the objective function has a simple structure it should be important to characterize the sets of these points, but an approach to this problem presently is not available, as far as we know.

The advantage of our method is that it is mathematically sound, it provides sequences with limit points, very frequently with a unique limit point and therefore, if the user is conscious of the difficulties of the problem, he can attempt to use this method for obtaining different solutions in practical applications and select that looking as the most appealing. In the next section we attempt to provide a few hints for helping the user in the choice of the parameters of the method and, in particular, of its initialization.

### 3. Image simulation

We model the images according to the model proposed in Snyder et al. (1994) for images acquired with a CCD camera, i.e. each pixel is affected by background (due to sky emission, dark current, etc.), photon counting noise (described by a Poisson distribution) and additive read-out noise (RON) described by a Gaussian distribution.

If the RON variance is  $\sigma^2$ , in the deconvolution process it can be approximated by a Poisson distribution with parameter  $\sigma^2$  if  $\sigma^2$  is added both to the detected images and the corresponding backgrounds (Snyder et al., 1995). Therefore all the pixel values of the detected images can be viewed as realizations of suitable Poisson random variables if in Eq. (1) we intend that  $\mathbf{g}_j, \mathbf{b}_j$  have been modified according to this approach. Therefore, in our numerical simulations we perturb the images with Poisson and additive Gaussian noise but in the deconvolution algorithms we use the images and backgrounds modified as above.

All the images and the PSFs considered in our numerical experiments are sized  $256 \times 256$  pixels in the single image case, with a pixel size of 15 mas, and  $512 \times 512$  pixels in the multiple image case, with a pixel size of 5 mas. Moreover all images, except one indicated in Sect. 4.1.1, are obtained by adding 10 frames in order to avoid saturation of the detector, as we discuss in the following, so that the variance of the RON will be  $10 \sigma^2$ .

#### 3.1. Single image simulation

In this case we use two PSFs in K-band with  $SR = 0.81$  and  $0.62$  respectively, modeling the optics of a single mirror of LBT, with diameter 8.4 m, and the effect of the adaptive optics system FLAO using the power spectrum of the wavefront residual of the AO correction as measured at the telescope (Esposito et al., 2012). To the noise-free image, obtained by convolving the object with one of these PSFs, a background in K-band is added

and the result is corrupted with Poisson and additive Gaussian noise. In order to avoid saturation of the detector (a maximum number of  $5 \times 10^4$  photons per pixel is assumed in a single frame) the image is obtained by co-adding  $n$  frames. More precisely, in the case of a stellar system the procedure for image generation is the following.

- We establish the coordinates of the stars and we fix their magnitudes in K-band.
- We compute the integration time which does not produce saturation of the detector by taking into account the collection area of the telescope, the overall efficiency of the acquisition system (assumed equal to 30%), and the flux of the brightest star multiplied by the peak value of the PSF. This is the integration time of a single frame and is used for computing the number of frames  $n$  required for obtaining an acceptable SNR for all the stars of the system.
- We generate noise-free images by shifting, with sub-pixel precision, the PSF to the positions of the stars and adding these shifted PSFs, each one weighted with a weight corresponding to the magnitude and the total observation time.
- These images are perturbed by adding a background in K-band, corresponding to about 13.5 mag arcsec<sup>-2</sup>, and by corrupting the results with Poisson and additive Gaussian noise (RON); the variance of the RON is  $n\sigma^2$ , thus corresponding to the RON of  $n$  frames; we take  $\sigma = 10 e^-/px$ .

#### 3.2. Multiple image simulation

As concerns the simulation of LN images, we recall that the instrument combines in a Fizeau mode the beams coming from the two mirrors of LBT whose center-to-center distance is about 14.4 m. Therefore the maximum baseline available is 22.8 m and the resolution achievable by a single LN image is that of a 22.8 m telescope in the direction of the baseline and that of a 8.4 m telescope in the orthogonal direction. For a given orientation the PSF of LN looks as that of a 8.4 m telescope, modulated by the interference fringes, orthogonal to the direction of the baseline. In order to get a more uniform resolution one must acquire and combine different images with different orientations of the baseline.

It is important to remark that the orientation of the fringes does not depend on the orientation of the baseline because the camera is rotating with the baseline and therefore the fringes have always the same direction (for instance the vertical one) in the image array. In other words two images of the same scientific object with two different orientations of the baseline correspond to two rotated versions of that object. This specific feature implies that one should introduce rotation matrices in the formulation of the problem. However we verified that the computation of hundreds or thousands of rotations in hundreds or thousands of inner iterations introduces large computational errors. Therefore we considered the approach which consists in derotating the images in such a way that they correspond to aligned versions of the object  $\mathbf{f}$ . The price to be paid is that the derotation of discrete images modifies their statistical

properties. In order to estimate this effect we considered the rotation of a constant array perturbed by Poisson noise. We found the following results:

- before rotation the histogram of the array is a Gaussian with the same mean and variance; after a rotation based on spline interpolation the histogram is still a Gaussian with the correct mean but a smaller variance;
- the support of the autocorrelation of the rotated image is a  $3 \times 3$  square;
- if we use a different rotation approach which consists in attributing the value of a pixel before rotation to the pixel with maximum overlapping after rotation (nearest neighbor approximation), the statistics is preserved but the quality of the image is degraded.

As a consequence of this analysis we decided to use in the approach derotated images.

The procedure adopted in our numerical experiments is similar to that used in the case of a single image. We consider two sets of PSFs in K-band with SR respectively 0.77 and 0.46, corresponding to orientation angles of the baseline indicated as  $0^\circ$ ,  $60^\circ$  and  $120^\circ$ , all with vertical fringes (for simplicity we take the same SR for the three orientations). The first PSF of each set has been generated by means of the software package LOST (Arcidiacono et al., 2004), the second by reflecting the first one with respect to the central line and the third by taking the arithmetic mean of the first two. In this way the three PSF of each set have exactly the same SR. Then the generation of the corresponding LN images is similar to that of the single image case by modifying the first item as follows.

- We establish the coordinates of the stars corresponding to the observation at  $0^\circ$  and we compute, with sub-pixel precision, their coordinates if the system is rotated by  $60^\circ$  and  $120^\circ$  respectively.

The rest of the procedure is unchanged and applied to the three images but at the end we must add the following item.

- The images corresponding to  $60^\circ$  and  $120^\circ$  are derotated in order to align the object in the three images and three arrays containing the object are extracted from the full images.

The derotated images are used in the definition of the objective function and in the blind algorithm, which therefore will produce derotated PSFs.

## 4. Numerical results

In order to evaluate the quality of the reconstructions obtained with our blind method we need some figures of merit.

As concerns the reconstruction of a binary we consider the relative absolute error on the magnitudes of both stars while in

the case of a stellar system we consider a magnitude average relative error (MARE) defined by

$$MARE = \frac{1}{q} \sum_{i=1}^q \frac{|m_i - \tilde{m}_i|}{\tilde{m}_i}, \quad (9)$$

where  $q$  is the number of stars and  $m_i$ ,  $\tilde{m}_i$  are respectively the reconstructed and the true magnitudes.

As concerns PSF reconstruction, in the case of single image we consider the root-mean-square error with respect to the true one, defined as usual in terms of the  $\ell_2$  norm of their difference. In the case of LN images generated according to the previous procedure, since the blind algorithm produces a set of three PSFs, two of them being derotated with respect to the ones used for generating the images, for comparison we must derotate the original ones. If we denote as  $\tilde{K}_j$  the derotated original PSF, then we measure the quality of the reconstruction by means of the root-mean-square error (RMSE)

$$\rho_j = \frac{\|K_j - \tilde{K}_j\|}{\|\tilde{K}_j\|}, \quad (10)$$

where  $K_j$  is the reconstructed PSF and  $\|\cdot\|$  denotes the usual  $\ell_2$ -norm.

### 4.1. Binary systems

We first consider the simple case of binary systems. More precisely we consider nine cases by varying both separation and magnitude of the stars. By keeping fixed the magnitude of the primary, i.e.  $m_1 = 15$ , we take for the magnitude of the secondary  $m_2 = 15, 16$  and  $17$ . Moreover for each choice we consider three possible angular separations:  $d = 60, 120$  and  $240$  mas in the single image case and  $d = 20, 40$  and  $80$  mas in the LN case. In both cases the first separation corresponds to the resolution limit of the instrument while the last is four times larger. In all cases, as described in the previous section, we compute the integration time of a frame in such a way that the number of counts in the image pixel corresponding to the position of the primary does not exceed  $5 \times 10^4$ . As stated in the previous section, we consider 10 frames per image, both in the single and in the multiple image case, so that the peak value of the photons is about  $5 \times 10^5$  for all images. Since in the case of LN we have three images, in this case the SNR is higher than in the single image case.

In Fig. 1 we show the images of the binaries with  $m_1 = m_2 = 15$  and different angular separations; in the first row those of the single image case and in the second row those of the multiple image case corresponding to the  $0^\circ$  baseline, all obtained with the PSF with the highest SR. The difficulty in reconstructing the binary with separation  $d = 20$  mas is obvious.

#### 4.1.1. Single image

For the convenience of the reader we give the computed integration time avoiding saturation in a single frame: 40 sec for SR = 0.81 and 52 sec for SR = 0.62. As already stated the images are obtained by adding 10 frames. These are the input images of the blind algorithm together with the value of the background.

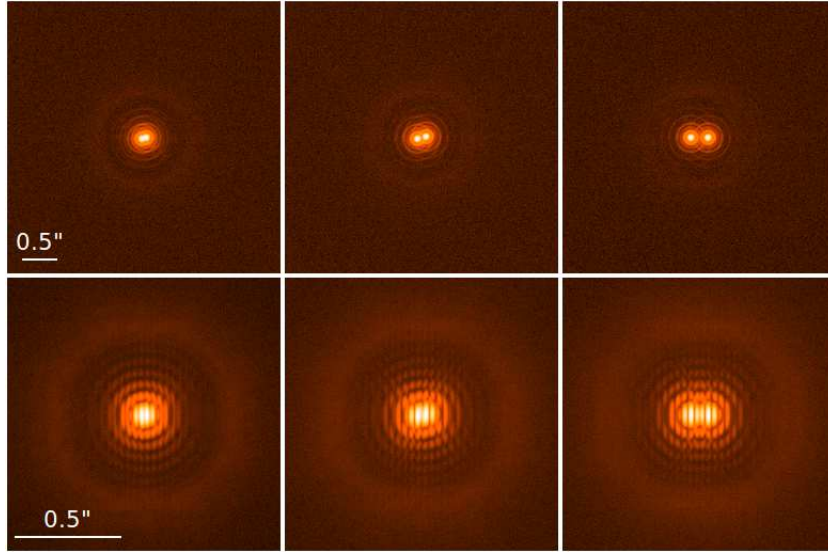


Figure 1: Examples of input images of binaries with magnitudes  $m_1 = m_2 = 15$ . In the first row those of the single image case, corresponding to PSF with  $SR = 0.81$ : from left to right, angular separation of 60, 120 and 240 mas. In the second row those of the multiple image case, corresponding to the PSF with  $SR = 0.77$ : from left to right, angular separation of 20, 40 and 80 mas. These images correspond to the first orientation of the baseline and only the central part of the images  $256 \times 256$  is displayed. In the two other orientations the binaries appear rotated by 60 and 120 degrees respectively. Images are displayed in log scale. The length corresponding to 0.5 arcsec is also indicated.

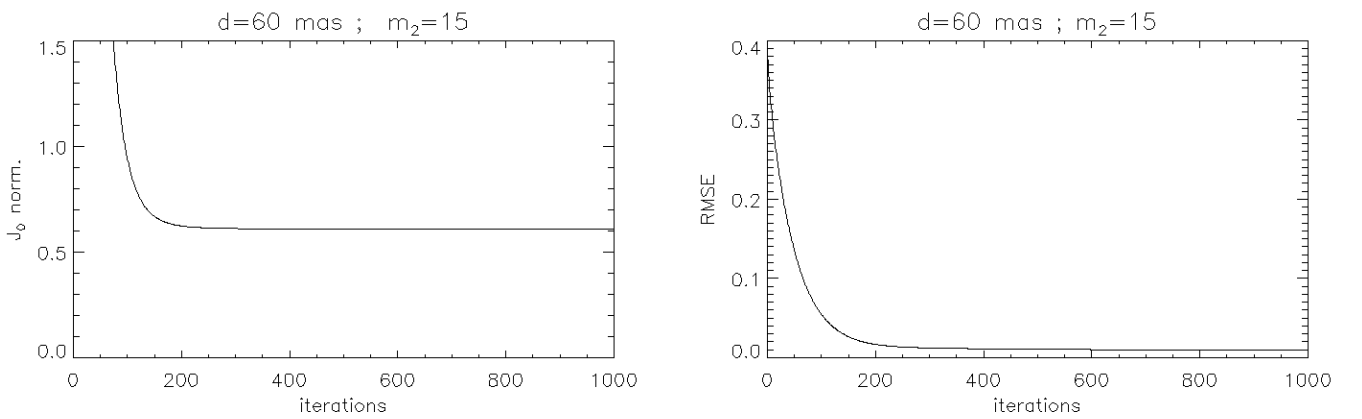


Figure 2: Behaviour, as a function of the number of iterations, of the normalized objective function (left panel) and of the RMSE on the PSF (right panel). The parameters of the binary are indicated in the figure. The plots refer to the PSF with  $SR = 0.81$ .

In a first attempt we use the initialization already used in Prato et al. (2013) and in other papers, namely a constant array for the object and the autocorrelation of the diffraction-limited PSF for the PSF. Indeed, this initialization has produced very promising results in our previous paper, where a much higher SNR was assumed. We use 1000 outer iterations in the case  $SR = 0.81$  and 2000 outer iterations in the case  $SR = 0.62$ . Indeed in the case of a lower SR we have a lower quality of the images and, presumably, a larger number of iterations is required. As concerns the inner iterations, as in Prato et al. (2013) we use 50 SGP iterations for the object and one SGP iteration for the PSF.

In Table 1 we give the results obtained with the previous choice. As a first remark, the binaries and the PSFs are reconstructed satisfactorily in all cases except the closest binaries ( $d = 60$  mas) with different magnitudes. Indeed, the indication 100% in the column for  $\Delta m_2/m_2$  means that the method reconstructs only one star, which sometimes is not exactly in the position of the primary but slightly shifted in the direction of the secondary. Since its magnitude is computed using a  $3 \times 3$  square centered on the true position of the primary, the error on its magnitude is, in general, not too large. On the other hand the error on the PSFs is very large, as one should expect since the secondary is missed. This point deserves further investigation.

In Fig. 2 we show, in a particular case, the behaviour of the normalized objective function, defined by  $2J_0/N^2$  with  $J_0$  given in Eq. (1) (with  $p = 1$ ), and of the RMSE on the PSF as functions of the number of iterations. Similar behaviors are obtained in all cases where a sensible result is obtained. This result suggests that presumably convergence is reached after 1000 iterations even if, as previously discussed, it is difficult to establish numerically the convergence of a sequence.

A second remark is that, according to statistical properties of Poisson random variables, if we compute the value of the normalized objective function by inserting in Eq. (1) the noisy and the noise-free images we should obtain a value very close to 1 (Bertero et al., 2010; Zanella et al., 2009). This is just what we obtain using our simulated images (this result also demonstrates the accuracy of the approximation of the RON with a Poisson random variable). However the limiting values of the normalized objective function obtained in our experiments are definitely smaller than 1, an effect already remarked in our previous paper.

Coming back to the problem of the unresolved binaries, we point out that, if we deconvolve the images using the PSF used for their generation (*inverse crime*) all the binaries are correctly reconstructed with small errors on their magnitudes. Therefore the failure of our experiment may be due to a failure of the method or to an inappropriate initialization or to inappropriate choices of the internal iterations.

Several attempts with different numbers of internal iterations did not improve the results. Therefore we searched for an initial PSF with a SR value closer to the correct one and with the property of being band-limited with the band of the LBT mirror. A possible choice is obtained by means of the diffraction-limited PSF of LBT, let us say  $\tilde{K}$ , by looking for an initial guess  $K^{(0)}$  of

the following form

$$K^{(0)} = \frac{1}{1 + \omega N^2} (\tilde{K} + \omega) \quad (11)$$

which is band-limited and satisfies the normalization condition. The constant  $\omega$  should be selected in such a way that  $K^{(0)}$  has the correct SR value, i.e.  $\max(K^{(0)}) = SR \max(\tilde{K})$ . We obtain

$$(SR N^2 \max(\tilde{K}) - 1)\omega = (SR - 1) \max(\tilde{K}) \quad (12)$$

and, by neglecting 1 with respect to the first term in the l.h.s. of this equation, we obtain  $\omega = (1 - SR)/(SR N^2)$ .

The results obtained with this initialization, using again 50 SGP iterations for the object and one for the PSF, are reported in Table 2. Since the convergence is slower than in the previous case we use 2000 outer iterations for  $SR = 0.81$  and 3000 iterations for  $SR = 0.62$ .

By comparing the results reported in the two tables we remark that the two different initializations provide very similar results in all cases where they succeed or they fail; in other words they provide sequences of iterations which presumably converge, even if with a different rate, to the same point, which is a stationary point of the objective function. Obviously we believe that it is also a minimizer. In the case of separation 60 mas and  $m_2 = 16$  the algorithm, equipped with the new initialization, is able to reconstruct the binary and the PSF with a satisfactory accuracy for both values of SR. We remark that the value of the objective function is higher than that corresponding to the result provided by the first initialization, which is not correct. This fact clearly indicates the existence of several stationary points or minimizers or both. Of course it should be nice to establish that the result of the first initialization is a stationary point and that of the second a minimizer; but, as already remarked such a verification is practically impossible. Finally, in the case  $m_2 = 17$  also the new initialization is unable to provide the correct results.

The results obtained in the multiple image case and described in the next subsection suggest that this negative result may be due to an insufficient value of the SNR. Therefore, in the case  $m_2 = 17$  we generated an image which is the sum of 30 frames (we point out that, as already remarked, in the considered multiple image case we have three times the photons of the single image case). Using again 2000 iterations, we find that the algorithm, with the second initialization, can resolve the binary in the case  $SR = 0.81$  (even if with a large reconstruction error, about 9 %, on the PSF) but not in the case  $SR = 0.62$ .

However in these difficult cases we observe a new phenomenon: even if in the limit the results are not satisfactory, the PSF reconstruction error exhibits a minimum before convergence. If we consider the reconstructions corresponding to these minima, then, in the case of the first initialization, the minima do not correspond to a situation where the binary is resolved. On the other hand, in the case of the second initialization, the binary is resolved for both SR values, with a 2.03 % PSF error in the case  $SR = 0.81$  (574 iterations) and a 7.13 % error in the case  $SR = 0.62$  (1739 iterations). Such a result presumably indicates the need of introducing a regularization



Table 1: Single image case - Binary reconstructions provided by the algorithm initialized with the autocorrelation of the diffraction-limited PSF. In the first column the value of the SR, in the second the angular separation, in the third the magnitude of the secondary, in the fourth and fifth the errors on the magnitudes of the two stars. In the subsequent column we give the RMSE for the reconstructed PSF. Finally in the last two columns we give the value of the normalized objective function, defined by  $2J_0/N^2$ , as computed at the end of the iterations, and the number of outer iterations.

SR	d (mas)	$m_2$	$\Delta m_1/m_1$	$\Delta m_2/m_2$	RMSE	$J_0$ norm.	IT
0.81	60	15	0.05%	0.03%	0.94%	0.6071	1000
		16	2.37%	100%	40.41%	0.5549	1000
		17	0.99%	100%	16.77%	0.5964	1000
	120	15	<0.01%	<0.01%	0.76%	0.6047	1000
		16	0.03%	<0.01%	1.11%	0.6296	1000
		17	0.03%	0.17%	1.40%	0.6254	1000
	240	15	<0.01%	<0.01%	0.79%	0.5999	1000
		16	0.02%	0.03%	0.83%	0.6273	1000
		17	<0.01%	0.04%	1.17%	0.6229	1000
0.62	60	15	0.18%	<0.01%	1.08%	0.5338	2000
		16	2.31%	100%	34.37%	0.4635	2000
		17	1.05%	100%	16.87%	0.4983	2000
	120	15	0.15%	0.14%	1.04%	0.5261	2000
		16	0.02%	0.01%	1.28%	0.5419	2000
		17	0.04%	0.25%	1.59%	0.5329	2000
	240	15	0.04%	0.04%	1.00%	0.5309	2000
		16	<0.01%	0.06%	1.13%	0.5537	2000
		17	0.05%	0.36%	1.80%	0.5361	2000

Table 2: Single image case - Binary reconstructions provided by the algorithm initialized with the diffraction-limited PSF plus a constant selected for satisfying the SR constraint (see the text). The structure of the Table is the same of Table 1.

SR	d (mas)	$m_2$	$\Delta m_1/m_1$	$\Delta m_2/m_2$	RMSE	$J_0$ norm.	IT
0.81	60	15	0.02%	0.04%	0.82%	0.6067	2000
		16	0.09%	0.16%	2.05%	0.6237	2000
		17	1.01%	100%	17.08%	0.5956	2000
	120	15	<0.01%	<0.01%	0.77%	0.6046	2000
		16	0.02%	<0.01%	1.09%	0.6294	2000
		17	0.02%	0.15%	1.35%	0.6253	2000
	240	15	<0.01%	<0.01%	0.80%	0.5989	2000
		16	0.02%	0.02%	0.82%	0.6271	2000
		17	<0.01%	0.02%	1.12%	0.6227	2000
0.62	60	15	0.02%	<0.01%	1.11%	0.5333	3000
		16	0.12%	0.25%	2.64%	0.5354	3000
		17	1.05%	100%	16.87%	0.4983	3000
	120	15	0.01%	0.01%	1.06%	0.5258	3000
		16	0.02%	<0.01%	1.26%	0.5419	3000
		17	0.04%	0.25%	1.58%	0.5329	3000
	240	15	0.03%	0.03%	0.99%	0.5304	3000
		16	<0.01%	0.06%	1.12%	0.5537	3000
		17	0.05%	0.36%	1.80%	0.5361	3000

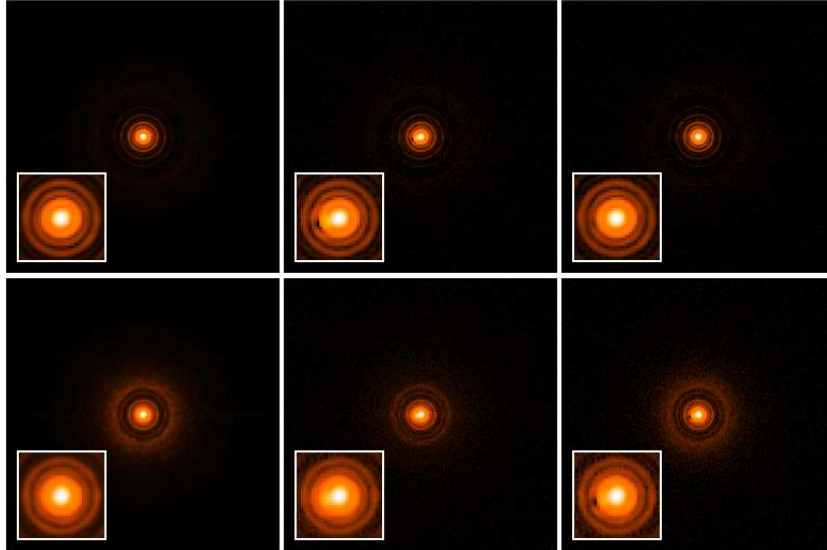


Figure 3: Single image case - PSF reconstruction in the case of the binary with  $d = 60$  mas and  $m_2 = 17$ . The input image is the sum of 30 frames (see text). These PSFs correspond to the minima of the reconstruction error. First column: the true PSF with SR = 0.81 (top) and SR = 0.62 (bottom). Second column: PSF reconstruction provided by the algorithm initialized with the autocorrelation of the diffraction-limited PSF. Last column: PSF reconstruction provided by the algorithm initialized with the diffraction-limited PSF plus a constant. In each panel we also show a zoom of the core of the PSF which makes evident artifacts due to the secondary. All images are displayed in log scale.

of the PSF in the objective function, at least for treating the most difficult cases. In Fig. 3 we show the reconstructions of the PSF corresponding to the minimum reconstruction errors. Artifacts due to the missed secondary are visible in the case of the first initialization and also in the case SR = 0.62, since the reconstructed secondary is fainter than the true one.

#### 4.1.2. Multiple images

In this case the integration time of a nonsaturated frame is 95 sec for SR = 0.77 and 167 sec for SR = 0.46. For each binary and orientation angle we consider again 10 frames, so that we have approximately the same number of photons in all images.

We preliminarily remark that, if we compute the value of the normalized objective function (which is now given by  $2J_0/3N^2$ ) by inserting in Eq. (1) the noisy and the noise-free images before derotation, we expect to obtain a value very close to 1 and this is just what we obtain. But this is not true if we compute the same quantity using the derotated images. Indeed, for the nine binaries as well as for the other objects, we always obtain a smaller value, namely 0.63. Since this value is independent of the object and PSFs, this effect is clearly due to the modification of the statistical properties of the data introduced by the derotation, as briefly discussed in Sect. 3.2. In any case the limiting values of the normalized objective function obtained in our experiments are definitely smaller than the values corresponding to the input objects and images, an effect already remarked in the previous case.

As in the single image case we first use as initialization a constant array for the object and the autocorrelations of the ideal PSFs for the three PSFs. The results of the reconstructions obtained with this initialization are reported in Table 3. We obtain that only when both stars have the same magnitude the method is able to reconstruct both the binary and the PSFs with suf-

ficient accuracy. When we have different magnitudes for the two stars the method is in general failing to reproduce the secondary, except in the case of separation  $d = 80$  mas; in this case a binary with difference of magnitude  $\Delta m = 1$  is also reconstructed. As in the single image case, the indication 100% in the column for  $\Delta m_2/m_2$  means that the method reconstructs an object which contains only one bright star (in one case the centroid is shifted one pixel in the direction of the secondary). These results show that, even if we have a higher SNR as already discussed, the multiple image case is more difficult than the single one.

If we deconvolve the derotated images using the derotated PSFs (this is not exactly an *inverse crime* because the images were generated with non derotated PSFs) all the binaries are correctly reconstructed with small errors on the magnitudes. Therefore the failure of our experiment may be due again to an inappropriate initialization (the autocorrelations of the ideal PSFs have a SR value of about 0.35, much smaller than the SR of the PSFs used in image generation) or to inappropriate choices of the internal iterations. Also in this case, as in Prato et al. (2013) and in the single image case, we use 50 SGP iterations for the object and one SGP iteration for each PSF. However several attempts with different numbers of internal iterations did not improve the results. Therefore, as in the single image case, we use as a new initialization of the PSFs the ideal PSFs of LN with the addition of a small constant selected in such a way to satisfy normalization and SR value. The results obtained with this initialization, using again 50 SGP iterations for the object and one for the PSFs, are reported in Table 4. Since the convergence is slower than in the previous case we use 2000 outer iterations.

With the new initialization the blind method succeeds in re-

Table 3: Multiple image case - Binary reconstructions provided by the algorithm initialized with the autocorrelations of the ideal PSFs. In the first column the value of the SR, in the second the angular separation, in the third the magnitude of the secondary, in the fourth and fifth the errors on the magnitudes of the primary and the secondary star. In the subsequent three columns we give the RMSE for the three PSFs. Finally in the last two columns we give the value of the normalized objective function, defined by  $2J_0/3N^2$ , as computed at the end of the iterations, and the number of outer iterations.

SR	d (mas)	$m_2$	$\Delta m_1/m_1$	$\Delta m_2/m_2$	RMSE $_{0^\circ}$	RMSE $_{60^\circ}$	RMSE $_{120^\circ}$	$J_0$ norm.	IT
0.77	20	15	0.28%	0.23%	1.52%	2.50%	1.87%	0.2241	1000
		16	2.12%	100%	30.00%	31.14%	21.79%	0.1706	1000
		17	0.87%	100%	14.93%	15.38%	11.00%	0.1890	1000
	40	15	0.30%	0.28%	1.66%	1.84%	2.56%	0.2647	1000
		16	2.20%	100%	41.65%	33.98%	33.80%	0.2049	1000
		17	0.58%	100%	14.78%	14.48%	15.90%	0.1954	1000
	80	15	0.20%	0.21%	1.09%	0.83%	0.83%	0.2180	1000
		16	0.18%	0.23%	1.27%	0.96%	0.99%	0.2164	1000
		17	0.87%	100%	19.28%	19.06%	19.04%	0.1893	1000
0.46	20	15	1.27%	1.19%	9.67%	9.69%	11.39%	0.1335	1000
		16	0.29%	100%	32.61%	33.10%	29.37%	0.0836	1000
		17	0.18%	100%	13.91%	14.12%	12.54%	0.0795	1000
	40	15	0.89%	0.88%	5.15%	5.62%	5.64%	0.1516	1000
		16	0.27%	100%	47.22%	41.54%	36.75%	0.1360	1000
		17	0.33%	100%	13.91%	14.67%	14.31%	0.0944	1000
	80	15	0.68%	0.68%	3.05%	2.60%	2.58%	0.1042	1000
		16	0.52%	0.60%	1.87%	1.43%	1.44%	0.0850	1000
		17	0.55%	100%	15.99%	15.97%	15.98%	0.0883	1000

Table 4: Multiple image case - Binary reconstructions provided by the algorithm initialized with the ideal PSFs plus a constant selected for satisfying the SR constraint (see the text). The structure of the Table is the same of Table 3.

SR	d (mas)	$m_2$	$\Delta m_1/m_1$	$\Delta m_2/m_2$	RMSE $_{0^\circ}$	RMSE $_{60^\circ}$	RMSE $_{120^\circ}$	$J_0$ norm.	IT
0.77	20	15	0.44%	0.34%	2.86%	4.23%	3.42%	0.2277	2000
		16	0.27%	0.21%	1.56%	1.82%	1.74%	0.2209	2000
		17	0.07%	1.10%	2.53%	2.70%	1.78%	0.2095	2000
	40	15	0.45%	1.03%	5.47%	4.61%	6.73%	0.2670	2000
		16	0.25%	0.39%	1.63%	2.85%	2.76%	0.2220	2000
		17	0.11%	0.73%	2.05%	2.78%	2.86%	0.2102	2000
	80	15	0.35%	0.35%	2.28%	1.51%	2.23%	0.2204	2000
		16	0.25%	0.26%	1.32%	1.06%	1.14%	0.2179	2000
		17	0.19%	0.40%	1.32%	1.02%	0.99%	0.2125	2000
0.46	20	15	0.80%	0.57%	4.02%	4.51%	6.83%	0.1037	2000
		16	0.38%	0.95%	3.76%	3.95%	2.52%	0.0811	2000
		17	0.07%	6.32%	9.05%	10.33%	6.29%	0.0697	2000
	40	15	0.64%	2.18%	11.23%	6.72%	8.73%	0.1409	2000
		16	0.49%	0.81%	2.21%	3.20%	2.99%	0.0837	2000
		17	0.02%	5.89%	8.70%	7.68%	8.84%	0.0716	2000
	80	15	0.56%	0.55%	8.54%	4.66%	4.64%	0.1100	2000
		16	0.57%	0.53%	1.99%	1.48%	1.49%	0.0846	2000
		17	0.48%	0.92%	2.36%	1.95%	1.96%	0.0785	2000

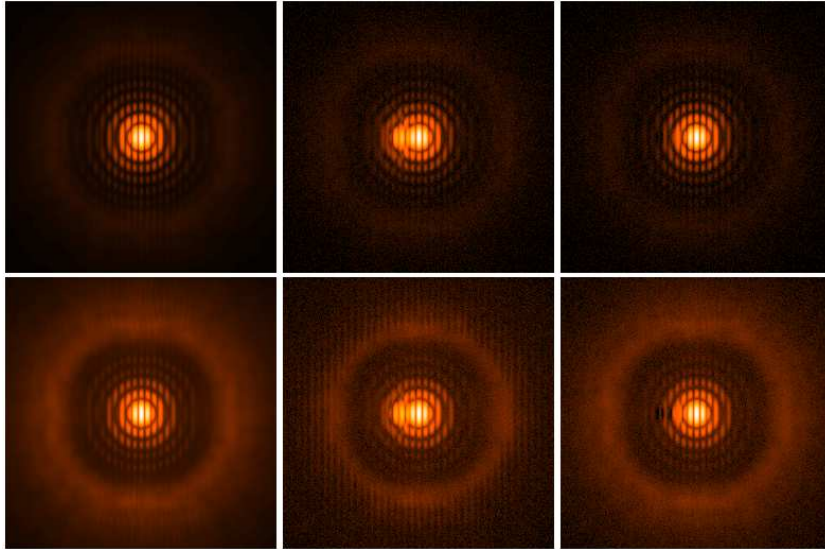


Figure 4: Multiple image case - PSF reconstruction in the case of the binary with  $d = 80$  mas and  $m_2 = 17$ . First column: the true PSF with SR = 0.77 (top) and SR = 0.46 (bottom). Second column: PSF reconstruction provided by the algorithm initialized with the autocorrelations of the ideal PSFs. Last column: PSF reconstruction if the algorithm is initialized with the ideal PSFs plus a constant. All images (only the central part  $256 \times 256$  is shown) are displayed in log scale and correspond to the first orientation of the baseline.

constructing all the binaries with sufficient accuracy as well as the PSFs. We can add that in most cases both the normalized objective function and the RMSE on the PSFs have a convergent behaviour while, in a few cases, the errors are still decreasing after 2000 iterations, thus indicating that a larger number of iterations could still improve the solution. A comparison of the values of the objective function reported in the two tables shows that, in some of the cases where the first initialization is failing, the values in Table 3 are smaller than the corresponding values in Table 4. This phenomenon was already observed in the single image case and means that different stationary points or minimizers are present.

A few more comments on the two tables. If one looks carefully at the reported results one can remark that, even if the results obtained with the second initialization are globally better than those obtained with the first one, this may not be true for particular cases (compare, for instance, the results for  $d = 40$  mas and  $\Delta m = 0$ ). Moreover, the errors obtained with the second initialization do not vary in a regular way with the variation of angular distance and difference of magnitude. These behaviors can be due to the fact that 2000 iterations may not be sufficient for assuring convergence of the method in the case of the second initialization. We did not push further the iterations because in the case of three  $512 \times 512$  images the computation time is considerable. By assuming possible fluctuations due to insufficient number of iterations, a reasonable conclusion seems to be that, as in the single image case, the two initializations lead to the same limit point when the first one is successful.

In Fig. 4 we show an example of reconstructions of the PSF at  $0^\circ$ , for both SR values, when the unknown object is a binary with  $d = 80$  mas and  $m_2 = 17$ . From the reconstructions displayed in the second column and obtained by initializing with the autocorrelations of the ideal PSFs, it is evident that they

contain a contribution coming from the secondary, while this contribution is practically absent in the reconstructions obtained with the other initialization and displayed in the third column.

#### 4.2. Star clusters

In a second experiment we consider two models of star cluster. The first is already considered in Prato et al. (2013) and is based on an image of the brightest stars of the Pleiades open cluster; for this reason, we call it “open star cluster”. It consists of nine stars that we take, in this paper, with magnitudes ranging from 14.4 to 17.1. In the single image case, the minimum distance between two stars is 120 mas, while the maximum distance is 1434 mas, with a mean distance of about 690 mas. In the multiple image case, considering the different pixel scale, we reduce of one third all the distances.

As a second example we consider a model that we call “globular star cluster”. For simplicity, only 150 stars are considered within the field of view, representing a very low crowding condition. The positions of the stars are randomly computed following a Gaussian distribution around the center of the image (with a standard deviation of about 450 mas in the single image case and of about 150 mas in the multiple image case); similarly the magnitudes of the stars are randomly distributed around  $m = 16$  with a standard deviation of about 0.4. It turns out that the brightest star of the cluster has  $m = 14.8$ .

Again, we limit the maximum number of counts in each frame to  $5 \times 10^4$ , keeping fixed to 10 the number of frames. In Fig. 5 we show the images of the two star clusters provided by the PSFs with the highest SR.

##### 4.2.1. Single image

In the case of the “open star cluster”, the integration time of a single frame is 22 sec for SR = 0.81 and 29 sec for SR = 0.62

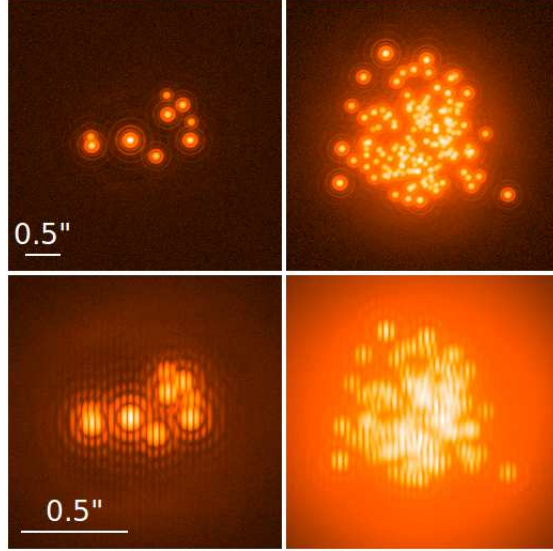


Figure 5: Top panels: the input images of the “open star cluster” (left) and of the “globular star cluster” (right) in the single image case with  $SR = 0.81$ . Bottom panels: the input images of the two clusters in the case of  $SR = 0.77$  and with  $0^\circ$  of the baseline (only the central part  $256 \times 256$  is shown). All images are displayed in log scale. The length corresponding to 0.5 arcsec is also indicated.

Table 5: Single image case - The reconstruction errors in the case of the two star cluster models. In the first column the “open cluster” is labelled by OC, while the “globular cluster” is GC. In the second column, we give the value of SR, while in the third column we give the initialization of the algorithm, denoting by A the autocorrelation of the diffraction-limited PSF and by C the diffraction-limited PSF plus a constant selected for satisfying the SR constraint (see the text). In the subsequent columns, we give the value of the magnitude average reconstruction error (MARE) defined in Eq. (9), and the RMSE for the reconstructed PSF. Finally in the last two columns we give the value of the normalized objective function, defined by  $2J_0/N^2$ , as computed at the end of the iterations, and the number of outer iterations.

Star Cluster	SR	Init.	MARE	RMSE	$J_0$ norm.	IT
OC	0.81	A	0.06%	0.84%	0.5993	2000
		C	0.06%	0.85%	0.5991	5000
	0.62	A	0.09%	1.22%	0.5165	4000
		C	0.09%	1.22%	0.5165	10000
GC	0.81	A	0.06%	0.87%	0.5123	3000
		C	0.06%	0.82%	0.4989	5000
	0.62	A	0.07%	1.07%	0.4622	6000
		C	0.07%	15.82%	0.5698	10000

while in the case of the “globular star cluster” these times are respectively 32 and 42 sec.

We applied to the four images our blind algorithm using both initializations introduced in the case of the binaries. The results are reported in Table 5. In the case of the “open star cluster” and both values of SR the two initializations seem to provide sequences of iterations converging to the same point. If we look at the image shown in the upper left panel of Fig. 5 we can observe that it contains sufficiently well-separated star images which can allow a good estimation of the PSF by the blind algorithm.

The situation is a bit different in the case of the “globular star cluster” and we can understand this fact if we look at the upper right panel of Fig. 5. In the case of the higher SR value both initializations lead essentially to the same result. The small differences may be due to different convergence rates and could be removed by a more accurate tuning of the number of iterations. On the other hand in the case of the lower SR ratio the first initialization, based on the autocorrelation of the diffraction-limited PSF, provides the best PSF reconstruction (also corresponding to a lower value of the objective function). It seems that the two initializations lead to two different stationary points. In conclusion, for this particular object one can state that the first initialization may provide a better result than the second one.

#### 4.2.2. Multiple images

In the case of the “open cluster” model, the integration time is 53 sec for  $SR = 0.77$  and 93 sec for  $SR = 0.46$ . On the other hand the integration time for the “globular cluster” images is 78 sec for  $SR = 0.77$  and 136.5 sec for  $SR = 0.46$ .

In both cases we apply our blind algorithm using the two initializations already used in the previous sections, with 50 inner SGP iterations for the object and one iteration for each PSF. The results obtained for the “open cluster” with the two initializations are given in the first two rows of Table 6 in the case  $SR = 0.77$  and in the following two rows those obtained in the case  $SR = 0.46$ . Similarly the results obtained for the “globular cluster” are given in the second half of the same table.

In the multiple image case the situation is more complex than in the single one, and this is not surprising since now we must reconstruct four blocks of variables. By looking at the results reported in Table 6 we see that the two initializations produce in all cases two sequences of iterations converging to distinct results. Even if, in some cases, the two values of the objective function are very close, the corresponding points are definitely different, thus implying the existence of several minimizers or stationary points with very close values of the objective functions.

It is interesting to remark that, while in the case of the binaries the best results are provided by the second initialization, now they are provided by the first one, based on the autocorrelations of the ideal PSFs. The highest reconstruction errors are obtained in the case of the lowest SR, as one should expect. We also remark that in the case of the second initialization we used a larger number of iterations because the convergence is slower than in the case of the first initialization. From the comparison

of the results obtained for the binaries with those obtained for the star clusters we deduce that the problem of the initial PSFs is essentially open; therefore, in the case of practical applications, one should try with different initializations, using also physical intuition in their choice.

As a final comment, all the values of the objective function corresponding to the best solutions are higher than those corresponding to the other ones.

## 5. Conclusions

In this paper we extend to the case of Fizeau interferometry a blind deconvolution method previously proposed for single aperture telescopes and we validate the method in both cases, called respectively multiple image and single image case.

It is well-known that the problem of blind deconvolution is extremely ill-posed and the introduction of constraints on PSF and object does not exclude the existence of several local minima, stationary points etc. In our approach the most significant constraint is the SR constraint on the PSFs, as suggested in Desiderà and Carbillet (2009). This constraint excludes the trivial solution of a delta function for the PSF and image for the object.

From our numerical analysis it turns out that the problem of Fizeau interferometry is more difficult than the problem of single aperture telescopes. The reason may be twofold. On one hand the number of variables to be reconstructed is larger and it is known that in the minimization of a nonconvex block-convex function the theoretical results are weaker when the number of blocks is greater than two. On the other hand the PSFs are very structured due to the presence of interference fringes so that if the initialization does not contain sufficient information on these structures it is difficult if not impossible to obtain acceptable results.

An astonishing feature already observed in the single aperture case and confirmed in the present paper is that very often the value of the objective function corresponding to a sensible solution is greater than the value corresponding to an unacceptable one. Obviously it is impossible to verify if these points correspond to local minima or to stationary points. In any case this result raises the issue if global minima, in case they were computable, provide sensible solutions or not.

In summary the results of this paper open a large number of problems; however we think that the proposed method, which has a sound mathematical foundation, is very flexible and can help to investigate these problems. Moreover, last but not least, it can be extended to introduce regularization terms both on the object and on the PSF (or PSFs) thanks to the high flexibility of SGP, which is the basic tool in our approach. It is sufficient to modify the scaling factor along the lines suggested in Lantéri et al. (2002). Obviously, in such a case, the additional problem arises of the choice of the regularization parameters.

We conclude by remarking that the IDL routines implementing our method are available on request and will be included in the forthcoming version of the Software Package AIRY (v.6.1) (Carbillet et al., 2014).

Table 6: Multiple image case - The reconstruction errors in the case of the two models of star cluster. The structure is similar to that of Table 5 but now we give the errors on the three PSFs and the normalized objective function is defined by  $2J_0/3N^2$ .

Star Cluster	SR	Init.	MARE	RMSE <sub>0°</sub>	RMSE <sub>60°</sub>	RMSE <sub>120°</sub>	J <sub>0</sub> norm.	IT
OC	0.77	A	0.35%	2.14%	4.28%	4.19%	0.3049	1000
		C	0.59%	4.16%	7.67%	7.62%	0.2997	5000
	0.46	A	0.81%	3.43%	6.07%	6.00%	0.1321	2000
		C	0.89%	3.74%	7.77%	7.81%	0.1237	10000
GC	0.77	A	0.38%	1.98%	3.46%	3.38%	0.7597	3000
		C	0.71%	11.00%	11.06%	12.97%	0.7459	5000
	0.46	A	1.04%	5.63%	9.69%	9.38%	0.3557	6000
		C	0.90%	25.81%	16.37%	17.94%	0.3043	10000

## Acknowledgements

This work has been partially supported by MIUR (Italian Ministry for University and Research), under the projects FIRB - Futuro in Ricerca 2012 (contract RBFR12M3AC) and PRIN 2012 (contract 2012MTE38N), and by INAF (National Institute for Astrophysics) under the project TECNO-INAf 2010 “Exploiting the adaptive power: a dedicated free software to optimize and maximize the scientific output of images from present and future adaptive optics facilities”. The Italian GNCS - INdAM (Gruppo Nazionale per il Calcolo Scientifico - Istituto Nazionale di Alta Matematica) is also acknowledged.

## References

## References

Arcidiacono, C., Diolaiti, E., Tordi, M., Ragazzoni, R., Farinato, J., Vernet, E., Marchetti, E., 2004. Layer-Oriented Simulation Tool. *Appl. Optics* 43 (22), 4288–4302.

Bailey, V. P., Hinz, P. M., Puglisi, A. T., Esposito, S., Vaitheeswaran, V., Skemer, A. J., Defrère, D., Vaz, A., Leisenring, J. M., 2014. Large binocular telescope interferometer adaptive optics: on-sky performance and lessons learned. In: Marchetti, E., Close, L. M., Véran, J.-P. (Eds.), *Adaptive Optics Systems IV*. Vol. 9148 of Proc. SPIE. p. 914803.

Barzilai, J., Borwein, J. M., 1988. Two-point step size gradient methods. *IMA J. Numer. Anal.* 8 (1), 141–148.

Bertero, M., Boccacci, P., 2000. Application of the OS-EM method to the restoration of LBT images. *Astron. Astrophys. Suppl. Series* 144 (1), 181–186.

Bertero, M., Boccacci, P., Desiderà, G., Vicidomini, G., 2009. Image deblurring with Poisson data: from cells to galaxies. *Inverse Probl.* 25 (12), 123006.

Bertero, M., Boccacci, P., La Camera, A., Olivieri, C., Carbillat, M., 2011. Imaging with LINC-NIRVANA, the Fizeau interferometer of the Large Binocular Telescope: state of the art and open problems. *Inverse Probl.* 27 (11), 113011.

Bertero, M., Boccacci, P., Talenti, G., Zanella, R., Zanni, L., 2010. A discrepancy principle for Poisson data. *Inverse Probl.* 26 (10), 10500.

Bertsekas, D., 1999. *Nonlinear programming*. Athena Scientific, Belmont.

Biggs, D. S. C., Andrews, M., 1998. Asymmetric iterative blind deconvolution of multi-frame images. In: Franklin, T. L. (Ed.), *Advanced Signal Processing Algorithms, Architectures, and Implementations VIII*. Vol. 3461 of Proc. SPIE. pp. 328–338.

Bonettini, S., 2011. Inexact block coordinate descent methods with application to non-negative matrix factorization. *IMA J. Numer. Anal.* 31 (4), 1431–1452.

Bonettini, S., Prato, M., 2010. Nonnegative image reconstruction from sparse Fourier data: a new deconvolution algorithm. *Inverse Probl.* 26 (9), 095001.

Bonettini, S., Prato, M., 2014. Accelerated gradient methods for the X-ray imaging of solar flares. *Inverse Probl.* 30 (5), 055004.

Bonettini, S., Zanella, R., Zanni, L., 2009. A scaled gradient projection method for constrained image deblurring. *Inverse Probl.* 25 (1), 015002.

Carbillat, M., Camera, A. L., Deguignet, J., Prato, M., Bertero, M., Aristidi, E., Boccacci, P., 2014. Strehl-constrained reconstruction of post-adaptive optics data and the Software Package AIRY, v. 6.1. In: Marchetti, E., Close, L. M., Véran, J.-P. (Eds.), *Adaptive Optics Systems IV*. Vol. 9148 of Proc. SPIE. p. 91484U.

Castello, M., Diaspro, A., Vicidomini, G., 2014. Multi-images deconvolution improves signal-to-noise ratio on gated stimulated emission depletion microscopy. *Appl. Phys. Lett.* 105 (23), 234106.

Csiszár, I., 1991. Why least squares and maximum entropy? An axiomatic approach to inference for linear inverse problems. *Ann. Stat.* 19 (4), 2032–2066.

Dai, Y. H., Fletcher, R., 2006. New algorithms for singly linearly constrained quadratic programming problems subject to lower and upper bounds. *Math. Program.* 106 (3), 403–421.

Desiderà, G., Anconelli, B., Bertero, M., Boccacci, P., Carbillat, M., 2006. Application of iterative blind deconvolution to the reconstruction of LBT LINC-NIRVANA images. *Astron. Astrophys.* 452 (2), 727–734.

Desiderà, G., Carbillat, M., 2009. Strehl-constrained iterative blind deconvolution for post-adaptive-optics data. *Astron. Astrophys.* 507 (3), 1759–1762.

Esposito, S., Riccardi, A., Fini, L., Puglisi, A. T., Pinna, E., Xompero, M., Briguglio, R., Quirós-Pacheco, F., Stefanini, P., Guerra, C. J., Busoni, L., Tozzi, A., Pieralli, F., Agapito, G., Brusa-Zappellini, G., Demers, R., Brynneel, J., Arcidiacono, C., Salinari, P., 2010. First light AO (FLAO) system for LBT: final integration, acceptance, test in Europe, and preliminary on-sky commissioning results. In: Ellerbroek, L. B., Hart, M., Hubin, N., Wizinowich, P. L. (Eds.), *Adaptive Optics Systems II*. Vol. 7736 of Proc. SPIE. p. 773609.

Esposito, S., Riccardi, A., Pinna, E., Puglisi, A. T., Quirós-Pacheco, F., Arcidiacono, C., Xompero, M., Briguglio, R., Busoni, L., Fini, L., Argomedo, J., Gherardi, A., Agapito, G., Brusa, G., Miller, D. L., Guerra Ramon, J. C., Boutsia, K., Stefanini, P., 2012. Natural guide star adaptive optics systems at LBT: FLAO commissioning and science operations status. In: Ellerbroek, L. B., Marchetti, E., Véran, J.-P. (Eds.), *Adaptive Optics Systems III*. Vol. 8447 of Proc. SPIE. p. 84470U.

Fish, D. A., Brinicombe, A. M., Pike, E. R., 1995. Blind deconvolution by means of the Richardson-Lucy algorithm. *J. Opt. Soc. Am. A* 12 (1), 58–65.

Grippo, L., Sciandrone, M., 1999. Globally convergent block-coordinate techniques for unconstrained optimization. *Optim. Method Softw.* 10 (4), 587–637.

Grippo, L., Sciandrone, M., 2000. On the convergence of the block nonlinear Gauss-Seidel method under convex constraints. *Oper. Res. Lett.* 26 (3), 127–136.

Herbst, T., Ragazzoni, R., Andersen, D., Boehnhardt, H., Bizenberger, P., Eckart, A., Gaessler, W., Rix, H.-W., Rohloff, R.-R., Salinari, P., Soci, R., Straubmeier, C., Xu, W., 2003. LINC-NIRVANA: a fizeau beam combiner for the large binocular telescope. In: Traub, W. A. (Ed.), *Interferometry for Optical Astronomy II*. Vol. 4838 of Proc. SPIE. pp. 456–465.

Holmes, T., 1992. Blind deconvolution of quantum-limited incoherent imagery: maximum likelihood approach. *J. Opt. Soc. Am. A* 9 (7), 1052–1061.

Hudson, H. M., Larkin, R. S., 1994. Accelerated image reconstruction using ordered subsets of projected data. *IEEE T. Med. Imaging* 13 (4), 601–609.

Lantéri, H., Roche, M., Aime, C., 2002. Penalized maximum likelihood image restoration with positivity constraints: multiplicative algorithms. *Inverse*

- Probl. 18 (5), 1397–1419.
- Leisenring, J. M., Hinz, P. M., Skrutskie, M. F., Skemer, A., Woodward, C. E., Veillet, C., Arcidiacono, C., Bailey, V., Bertero, M., Boccacci, P., Conrad, A., de Kleer, K., de Pater, I., Defrère, D., Hill, J., Hofmann, K.-H., Kaltenecker, L., La Camera, A., Nelson, M. J., Schertl, D., Spencer, J., Weigelt, G., Wilson, J. C., 2014. Fizeau interferometric imaging of Io volcanism with LBTI/LMIRcam. In: Rajagopal, J. K., Creech-Eakman, M. J., Malbel, F. (Eds.), *Optical and Infrared Interferometry IV*. Vol. 9146 of Proc. SPIE. p. 91462S.
- Lucy, L. B., 1974. An iterative technique for the rectification of observed distributions. *Astron. J.* 79, 745–754.
- Lucy, L. B., Hook, R. N., 1992. Co-adding images with different PSF's. In: Worrall, D. M., Biemesderfer, C., J., B. (Eds.), *Astronomical Data Analysis Software and Systems I*. Vol. 25 of A.S.P. Conference Series. pp. 277–279.
- Luo, Z.-Q., Tseng, P., 1992. On the convergence of the coordinate descent method for convex differentiable minimization. *J. Optim. Theory App.* 72 (1), 7–35.
- Powell, M. J. D., 1973. On search directions for minimization algorithms. *Math. Program.* 4 (1), 193–201.
- Prato, M., Cavicchioli, R., Zanni, L., Boccacci, P., Bertero, M., 2012. Efficient deconvolution methods for astronomical imaging: algorithms and IDL-GPU codes. *Astron. Astrophys.* 539, A133.
- Prato, M., La Camera, A., Bonettini, S., Bertero, M., 2013. A convergent blind deconvolution method for post-adaptive-optics astronomical imaging. *Inverse Probl.* 29 (6), 065017.
- Richardson, W. H., 1972. Bayesian based iterative method of image restoration. *J. Opt. Soc. Am.* 62 (1), 55–59.
- Snyder, D. L., Hammoud, A. M., White, R. L., 1994. Image recovery from data acquired with a charge-coupled-device camera. *J. Opt. Soc. Am. A* 10 (5), 1014–1023.
- Snyder, D. L., Helstrom, C. W., Lanterman, A. D., Faisal, M., White, R. L., 1995. Compensation for readout noise in CCD images. *J. Opt. Soc. Am. A* 12 (2), 272–283.
- Tsumuraya, F., Miura, N., Baba, N., 1994. Iterative blind deconvolution method using Lucy's algorithm. *Astron. Astrophys.* 282 (2), 699–708.
- Wilson, J. C., Hinz, P. M., Skrutskie, M. F., Jones, T., Solheid, E., Leisenring, J., Garnavich, P., Kenworthy, M., Nelson, M. J., Woodward, C. E., 2008. LMIRcam: an L/M-band imager for the LBT combined focus. In: Schoeller, M., Dauchi, W. C., Delplancke, F. (Eds.), *Optical and Infrared Interferometry*. Vol. 7013 of Proc. SPIE. p. 70133A.
- Zanella, R., Boccacci, P., Zanni, L., Bertero, M., 2009. Efficient gradient projection methods for edge-preserving removal of Poisson noise. *Inverse Probl.* 25 (4), 045010.